

# Electron gun for diffraction experiments off controlled molecules

Nele L. M. Müller,<sup>1</sup> Sebastian Trippel,<sup>1</sup> Karol Długolecki,<sup>1</sup> and Jochen Küpper<sup>1,2,3,\*</sup>

<sup>1</sup>Center for Free-Electron Laser Science, DESY, Notkestrasse 85, 22607 Hamburg, Germany

<sup>2</sup>The Hamburg Center for Ultrafast Imaging, University of Hamburg, Luruper Chaussee 149, 22761 Hamburg, Germany

<sup>3</sup>Department of Physics, University of Hamburg, Luruper Chaussee 149, 22761 Hamburg, Germany

(Dated: March 2, 2022)

A dc electron gun, generating picosecond pulses with up to  $8 \times 10^6$  electrons per pulse, was developed. Its applicability for future time-resolved-diffraction experiments on state- and conformer-selected laser-aligned or oriented gaseous samples was characterized. The focusing electrodes were arranged in a velocity-map imaging spectrometer configuration. This allowed to directly measure the spatial and velocity distributions of the electron pulses emitted from the cathode. The coherence length and pulse duration of the electron beam were characterized by these measurements combined with electron trajectory simulations. Electron diffraction data off a thin aluminum foil illustrated the coherence and resolution of the electron-gun setup.

Diffraction imaging is a promising approach to unravel the microscopic details of chemical processes through the recording of so-called molecular movies in the gas-phase, which trace the structural dynamics of individual molecules and nano-particles at the atomic level. Electron and x-ray diffraction are well established tools to investigate the structures of solid state samples [1], for example in transmission electron microscopy [2] or x-ray crystallography [3, 4]. Furthermore, electron diffraction has found broad application for gas-phase structure-determination in chemistry [5]. Recent developments have mainly focused on realizing time-resolved experiments in order to study structural dynamics, where x-ray and electron diffraction served as complementary approaches [6–11].

To be able to record structural changes during ultrafast molecular processes of small complex molecules in the gas phase, signals from many identical molecules have to be averaged. Gas-phase investigations pose the challenge that the sample might comprise different isomers and sizes [12]. In addition, the molecules in the gas phase are typically randomly oriented. It is therefore important to provide samples, which are as clean and defined as possible, to allow for experimental averaging over multiple electron pulses. Clean molecular samples can be generated by their spatial separation according to shape [13–15] and size [16]. Controlling the spatial orientation of the molecules leads to an enhancement of the information that can be retrieved from a diffraction pattern, as proposed theoretically [17–20] and demonstrated experimentally for x-ray [21, 22] as well as for electron diffraction [23, 24]. Strong alignment or orientation is generally necessary [11, 20] for three-dimensional structure reconstruction [24] and can be provided in cold supersonic molecular beams by strong-field laser alignment and mixed-field orientation [25–29]. The low density of these controlled gas-phase samples requires sources of large-cross-section particles or photons with large brightness, while still ensuring atomic resolution. Electron sources can meet these requirements even in table-top

setups.

The first sources for creating electron pulses short enough to study ultrafast processes in molecules or materials were dc electron guns. Here, electrons were created from metallic surfaces by short laser pulses and accelerated in dc electric fields [7, 8], yielding sub-picosecond electron pulses of moderate coherence and brilliance. Radio-frequency cavities allow for temporal compression of electron pulses through phase-space rotation, shortening the pulse duration to below 100 fs with electron numbers of  $10^6$  per pulse and electron spot sizes below 100  $\mu\text{m}$  [30]. Compact dc guns can achieve comparable properties by increasing the acceleration fields and reducing the path length, during which the electron pulse can expand [31–34]. Ultra-fast-single-electron sources [35] avoid the problem of space charges, but rely on very high repetition rates to achieve sufficient electron fluxes for diffractive imaging experiments. The use of ultra cold atoms as electron sources increases the coherence [36, 37]. Other possible sources for time-resolved electron diffraction are low energy electron setups [38] or laser-induced electron diffraction [39, 40].

If the molecular samples are prepared in the necessary strongly-controlled fashion, their densities are typically on the order of some  $10^8$  molecules/ $\text{cm}^3$  [21, 41]. Assuming Rutherford scattering, for the prototypical molecule 2,5-diiodobenzonitrile an effective cross section on the order of  $10^{-15}$   $\text{cm}^2$  can be derived for our experimental geometry and a beam stop blocking a solid angle of  $1.3 \times 10^{-3}$  sr. To align or orient the molecules, they are typically exposed to laser fields with intensities of 1 TW/ $\text{cm}^2$  [25], which can be achieved by focusing the ps-duration mJ-pulse-energy laser beam to 100  $\mu\text{m}$  [42]. For a 500  $\mu\text{m}$  thick molecular beam this results in an interaction volume of about  $5 \times 10^{-6}$   $\text{cm}^3$ . The number of molecules in this volume and the given cross section lead to an elastic scattering signal on the detector  $S_{\text{elastic}}^D$  of  $5 \times 10^{-9}$  per electron. In order to achieve a diffraction pattern containing some  $10^5$  scattered electrons on the detector within 24 hours, bright electron sources with  $10^9$

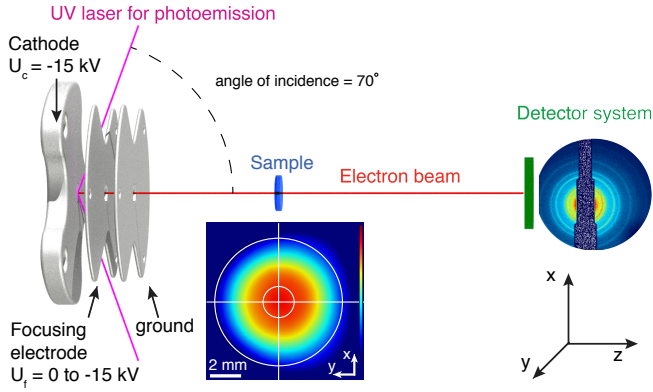


FIG. 1. Experimental scheme of the electron gun consisting of three electrodes in velocity-map-imaging-spectrometer configuration. After photoemission, the electrons were diffracted off an aluminum sample or were measured by a Faraday cup coupled to an electrometer. A multi-channel-plate detector with phosphor screen and a camera was used for position sensitive detection. The inset at the bottom depicts the potential between cathode and focusing electrode. To highlight the asymmetry the  $x = 0$  and  $y = 0$  axes as well as centered circles are shown to guide the eye.

electrons per second are needed. For experimental repetition rates on the order of 1 kHz [42], this corresponds to  $10^6$  electrons per shot with an electron beam focus size of approximately  $100\ \mu\text{m}$ . The setup presented here produced the necessary electron numbers and allowed for a characterization of the electron beam to ensure, for instance, the required transverse coherence length.

A schematic of the experimental setup is shown in Figure 1. The electrons were photo-emitted from a copper cathode *via* one-photon absorption after irradiation with short UV laser pulses. The pulses were generated by third-harmonic generation (THG) of 30-fs-duration near-infrared pulses from a Ti:Sapphire laser (TSL) system with a repetition rate of 1 kHz. Based on the pulse duration of the near-infrared laser pulse at the THG setup, and the dispersion in subsequent optical elements, we estimated a pulse duration of 370 fs for the UV light. The central wavelength was 265 nm with a spectral width of 4 nm. The light enters and exits the chamber through anti-reflection coated windows. The pulse impinged on the cathode under an angle of  $70^\circ$  to the surface normal of the cathode. The electrons were accelerated and focused by three electrodes in velocity-map imaging spectrometer (VMI) configuration. The applied potential at the cathode was  $U_c = -15\ \text{kV}$ . The voltage on the focusing electrode was varied between  $U_f = 0\ \text{kV}$  and  $-15\ \text{kV}$ . The third electrode was kept on ground potential. The asymmetric electrode shape allowed the laser beam to pass and impinge on the cathode. The holes within the electrodes were large enough to avoid clipping of the electron beam. On the one hand this reduced the back-

ground signal in diffraction experiments, as there was no electron scattering off the electrodes. On the other hand it allowed for steering the electron beam's position by changing the laser-spot position on the cathode. The voltage on the focusing electrode  $U_f$  determined the position of the electron beam focus along the  $z$  direction. The electrode configuration allowed to characterize the electron pulse by applying the corresponding voltages for spatial- and velocity-mapping [43–45]. It is possible to create electric fields that allow to either map the spatial distribution of the electrons at the cathode or their respective velocity distribution as a 2D projection onto the detector [43, 44]. The spatial distribution of the electron beam was recorded by a position sensitive detector consisting of a multi-channel-plate (MCP) with a phosphor screen and a CMOS camera (Optronis CamRecord CL600x2). The detection system was read out with a 1 kHz repetition rate, which allowed for single electron counting in the case of a few electrons per pulse. At large electron numbers, the gain of the detector had to be reduced to avoid damage of the MCP. With lower gain single electrons could not be resolved anymore. In order to reduce background from scattered light or other sources the detector can be gated. A Faraday cup connected to an electrometer (Keithley 6514 electrometer) was used to measure the electron number per pulse. To further characterize the electron pulses, we performed diffraction experiments with a thin aluminum foil on a TEM grid, which was introduced into the electron beam path. In this case the direct electron beam was blocked by a copper or aluminum beam block.

The electron gun was designed for ultra-high vacuum. Here, the final pressure was  $4 \times 10^{-9}$  mbar using a turbomolecular pump with pumping speed of 300 l/s, limited by outgassing from the cable of the Faraday cup and from PEEK material of the electron-gun insulators. This low pressure is essential when investigating thin gas-phase samples in order to reduce the scattering by background gas. We expect to achieve pressures of a few  $10^{-10}$  mbar in the final setup when replacing all PEEK insulators by MACOR or alumina.

In Figure 2 the electron number per pulse is shown for  $U_f = -13.2\ \text{kV}$  as a function of the laser pulse intensity for two laser polarizations. This focusing voltage corresponded to the focus of the electron beam being close to the detector surface. The number of electrons increased linearly with the laser power, as expected for a one-photon effect of 265 nm light with a spectral width of 4 nm on copper, which has a work function of 4.7 eV. No saturation was observed. The number of generated electrons depended on the laser polarization: For p-polarization (red curve, field vector in plane of incidence) more electrons were generated than for s-polarization (blue curve, field vector parallel to cathode surface). This is in accord with the reflectivity of copper being higher for s-polarized light than for p-polarized light, which was

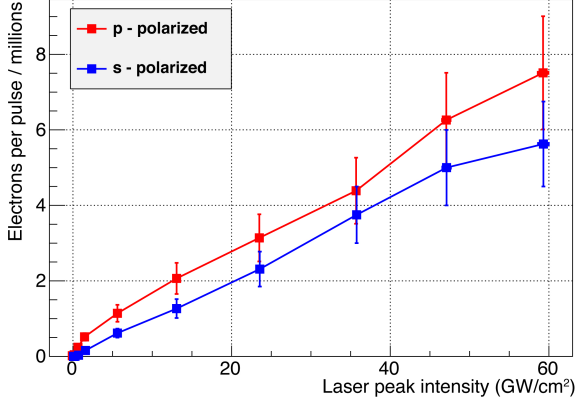


FIG. 2. Electron number as a function of laser peak intensity for p-polarized (red) and s-polarized (blue) laser light and a central laser wavelength of 265 nm.

confirmed by measuring the laser power for both polarizations after the cathode. Up to  $8 \times 10^6$  electrons per shot could be obtained, which is sufficient for the planned diffraction experiments on dilute gas-phase samples delivered by the controlled-molecules apparatus.

For a full characterization of the electron beam the electron spot size at the detector was measured for various focusing voltages  $U_f$ , including those for spatial- and velocity-mapping. In Figure 3 a the root-mean-square (RMS) spot size of the electron beam in  $x$  and  $y$  dimension,  $\sigma_x$  and  $\sigma_y$ , are plotted as a function of  $U_f$ . Here, the laser intensity was reduced to less than  $10 \text{ MW/cm}^2$  to create approximately five electrons per pulse from the cathode and, therefore, space charge effects were negligible. The spot size decreased with increasing  $U_f$  until it reached a focus, at the detector, for about  $U_f = -13 \text{ kV}$ . Raising  $U_f$  further led to a defocusing of the electron beam, i. e., the focus was placed before the detector. The exact voltage to place the focus onto the detector depends on the initial size of the electron cloud. The electron beam was broadened in  $x$  direction due to the large angle of incidence of the laser. Therefore, the foci in  $x$  and  $y$  dimension had slightly different focusing behavior.

In spatial imaging mode,  $U_f = -13.3 \text{ kV}$ , the spatial distribution of emitted electrons was mapped onto the detector, which is depicted as inset in Figure 3 a. In this case, all electrons, which started from a certain coordinate on the cathode hit a corresponding point on the detector, in first order independent of their momentum [44]. The magnification factor  $m_s$  for spatial imaging was calibrated in the experiment by translating the laser-focus spot on the cathode using the focusing lens. From a known displacement of the electron beam on the cathode  $\Delta x_C$  and the corresponding measured displacement of the electrons on the detector  $\Delta x_D$  a magnification factor of  $m_s = \Delta x_D / \Delta x_C = 3.9$  was determined. This agreed

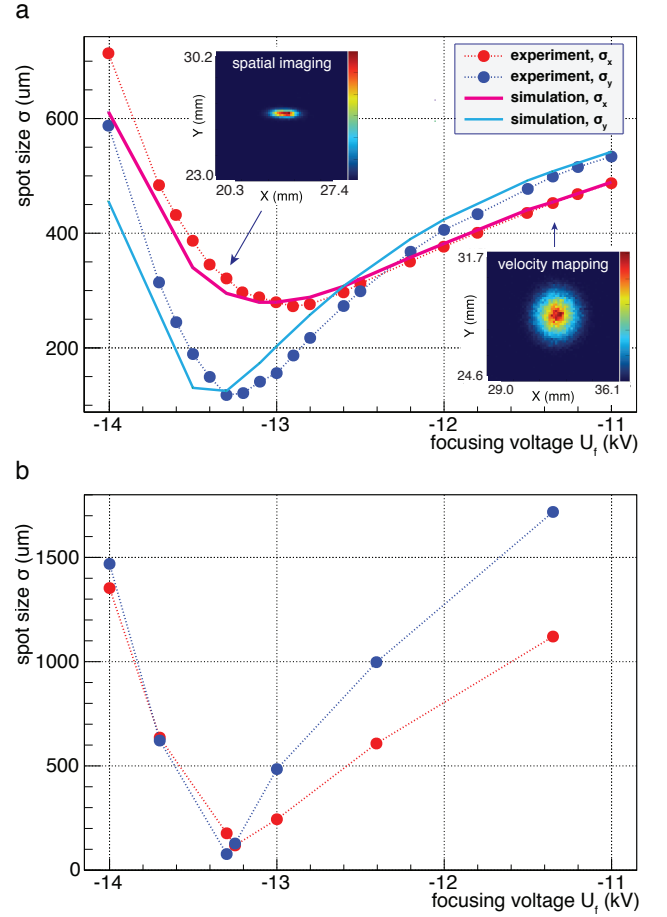


FIG. 3. Electron spot size on the detector for different focusing voltages for (a) a few and (b)  $2 \times 10^5$  electrons per pulse. Red and blue dots are experimental results corresponding to  $x$  and  $y$  directions, respectively. Magenta and cyan lines correspond to corresponding simulations in  $x$  and  $y$  dimension. The insets in (a) show detector images for spatial (left) and velocity map imaging (right).

with the simulated value. For simulations of electric fields and trajectories finite-element methods were used (COMSOL Multiphysics). The inferred RMS sizes of the electron beam at the cathode were  $\sigma_x = 85(3) \text{ }\mu\text{m}$  and  $\sigma_y = 31(1) \text{ }\mu\text{m}$ ; values in parenthesis depict one standard deviation. The difference in spread originated from the laser impinging on the cathode under an angle of incidence of  $70^\circ$ . The angle lead to an effective broadening of the photoemission laser by a factor of approximately three in  $x$  direction, while the  $y$  dimension was unchanged. Thus, the created electron beam was broader in  $x$  direction than in  $y$  direction on the cathode, which was confirmed in the spatial imaging measurements.

In velocity map imaging mode ( $U_f = -11.35 \text{ kV}$ ) the transverse velocity distribution was mapped onto the detector, which is shown as the second inset in Figure 3 a. The velocity spread was similar in both dimensions. With the simulated magnification factor of  $m_v = 0.9$  for velocity

mapping and a simulated electron time of flight of 4.1 ns an energy spread of  $\sigma_E = 0.1$  eV was obtained. This agrees well with the previously reported value  $\sigma_E = 0.13$  eV [46].

In order to characterize the electron beam further simulations and measurements at various focusing voltages  $U_f$  were performed. The spatial and velocity distribution of the electrons in  $x$  and  $y$  dimension could be retrieved from the experiment, but the corresponding values in  $z$  dimension had to be simulated. Electric fields were calculated using finite-element methods (COMSOL Multiphysics) and the electron trajectories in these fields were simulated using ASTRA [47]. The initial spatial distribution at the cathode was taken from the measurements described above. Together with a Fermi Dirac distribution for the one-photon emission, this led to the emittance values of  $\epsilon_x = 0.026 \pi$  mrad mm and  $\epsilon_y = 0.010 \pi$  mrad mm, and the energy spread in  $z$ -direction of  $\sigma_{E_z} = 0.2$  eV. Fitting the emittance to the transverse velocity distributions retrieved from VMI mode, while keeping  $\sigma_{E_z}$  constant, resulted in  $\epsilon_x = 0.029 \pi$  mrad mm and  $\epsilon_y = 0.012 \pi$  mrad mm, in good agreement with the values obtained from the Fermi Dirac distribution. Using the fitted input parameters, the overall dependence of the electron beam spot size at the detector on the focusing voltage was simulated. The results are depicted by the magenta and cyan lines in Figure 3a and are, again, in good agreement with the experimental results. This indicates that also the simulated  $\sigma_{E_z}$  was sensible. Due to the good agreement between experiment and simulation it is possible to deduce properties of the electron beam from the simulations, including size, coherence length and pulse duration, for its whole propagation. The coherence length  $L_c = \hbar \sigma_x / (m_0 c \epsilon)$ , with the electron mass  $m_0$  and the speed of light  $c$ , was determined using ASTRA [47]. At the sample position (11 cm downstream from the cathode)  $L_c$  was deduced to be 3 nm in  $x$ -dimension and 1.2 nm in  $y$ -dimension. The pulse duration at this position was simulated to be 1.4 ps.

Figure 3b shows the spot sizes for  $2 \times 10^5$  electrons per pulse, where space charges had a significant effect. For the detection of  $2 \times 10^5$  electrons per pulse in Figure 3b, the detector voltage had to be reduced and single electron detection was not possible. This implies that Figure 3a and b are only qualitatively comparable. A stronger asymmetry in velocity map imaging mode was observed than above. This could not be reproduced using a cylindrical symmetry in electric fields and initial velocities, which was a good approximation in the simulations for few electrons. Using finite-element simulations it was possible to qualitatively determine the origin of the asymmetry in the velocity map imaging mode, but a full simulation of all 3D trajectories for  $2 \times 10^5$  electrons was not possible due to too high computational cost. Simulations for few electrons showed that the trajectories of the electrons far off the central axis of the spectrometer were disturbed by the asymmetry of the electric field due to

the opening in the electrodes, see inset in Figure 1. This became more pronounced when space charges lead to a significant broadening of the electron distribution. In the case of  $2 \times 10^5$  electrons per pulse the radial distribution between the cathode and the focusing electrode was increased by an order of magnitude compared to the few electron case. This led to a larger magnification factor in vertical direction in velocity map imaging mode and, therefore, contributed to the asymmetry in the detector image. Secondly, the space charge effect itself led to an asymmetry in the velocity distribution, if the electron spot was asymmetric. For an ellipsoid with homogeneous charge density, the velocity in the direction of the shorter axis is higher [48]. In our case, the velocity distribution along  $y$  direction was larger, as the size of the cloud is smaller in this dimension. Simulating similar electron densities in smaller, but asymmetric volumes showed an asymmetric velocity distribution as well. The velocity was higher in the direction of the smaller expansion, corresponding to the  $y$  direction in the experiment. Both effects resulted in the vertical broadening of the electron pulse in velocity-mapping mode.

Simulations in cylindrical symmetry (ASTRA) for one million electrons per pulse provided an approximate value for the pulse duration at the sample position of 60 ps. Albeit this was much longer than in the case of a few electrons/pulse, it is sufficiently short for the diffractive imaging of aligned and oriented molecules, which we can routinely create and control for hundreds of picoseconds [42, 49].

A thin polycrystalline aluminum sample was used to test the electron-optical properties of the generated electron pulses, for instance, its coherence length and spatial resolution. The inset in Figure 4a shows a diffraction pattern for  $10^3$  electrons per pulse averaged over  $10^6$  pulses, i.e., about 15 min at 1 kHz. The electron beam was focused on the detector, which resulted in a nearly collimated beam at the position of the sample. The typical diffraction rings of a polycrystalline sample were observed [1]. The corresponding radial distribution as a function of momentum transfer  $s$  is plotted in Figure 4a. The peaks can be assigned to the allowed face-centered cubic crystal structure reflections for aluminum and the corresponding Miller indices ( $hkl$ ) are used to label the peaks [1].

The inset in Figure 4b shows a diffraction pattern averaged over  $10^3$  pulses ( $\sim 1$  s) with  $10^6$  electrons per pulse. A 6-mm-wide beam stop was used, but the MCP voltage still had to be reduced to avoid damaging the detector due to many electrons scattered to small  $s$ . Reducing the MCP voltage reduces the gain of the detector system, i.e., the signal on the camera per impinging electron. With this lower gain single, or a few, electrons could not be detected anymore. Therefore, the peak intensities in Figure 4a and b cannot be compared quantitatively. Diffraction peaks are still visible in Figure 4b, except for the largest  $s$  where



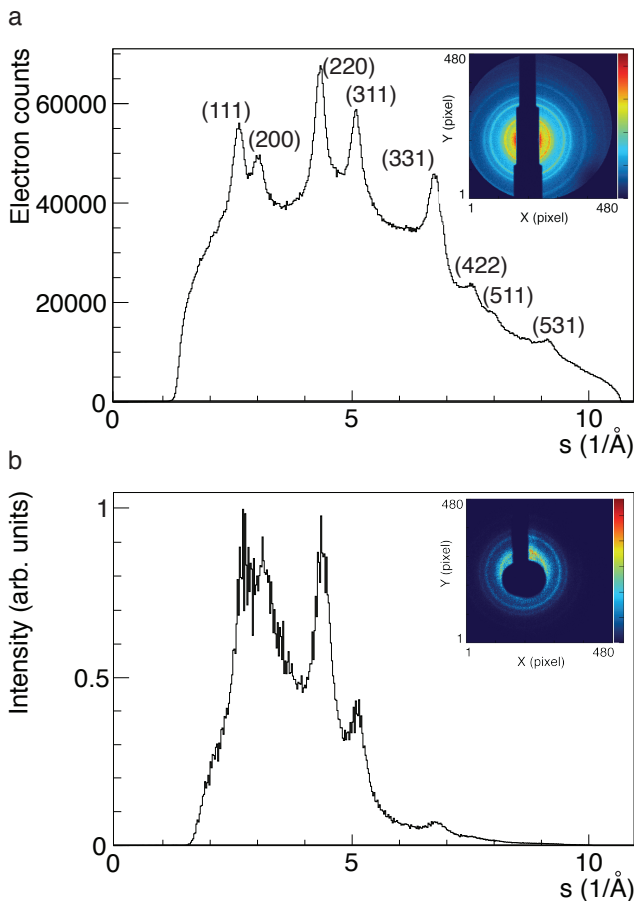


FIG. 4. Radial scattering intensity for aluminum for (a)  $10^3$  and (b)  $10^6$  electrons per pulse. Peaks are labeled with Miller indices ( $hkl$ ). The insets show the corresponding diffraction patterns.

the electron number and the gain were too small. This implies that the transverse coherence of the electron pulses were larger than 234 pm, while approximately 1 nm was expected from simulations. The spatial resolution of the imaging experiment was better than 234 pm, the interatomic distance corresponding to the (111) reflection in the diffraction pattern of aluminum. The restriction in resolution due to the lower detector gain will not occur in the envisioned gas-phase experiments, as the sample density will be much smaller. Thus, single-electron detection will also be possible for large electron numbers per pulse.

Using the implemented spectrometer it was possible to experimentally obtain the emittance, i. e., the initial transverse spatial and velocity distributions of the electrons. The combination with simulations allowed for the deduction of further values, such as the coherence length and pulse duration of the propagated electron pulses. Compared to other sources with time resolutions on the order of 1 ps or below [7, 8], our setup did produce electron pulses with 1.5 ps duration for few elec-

trons/pulse. More importantly, our table-top setup allows for a stable production of  $> 10^6$  electrons/pulse at a repetition rate of 1 kHz with an estimated pulse durations of 60 ps. Nevertheless, due to the negligible cross-sections radiation damage can be neglected even on these long timescales. For the prototypical 2,5-diiodobenzonitrile molecule the effective electron-impact-ionization cross section is about  $10^{-16}$  cm<sup>2</sup>, whereas the effective elastic-scattering cross section is  $10^{-15}$  cm<sup>2</sup>. For  $10^6$  electrons per pulse, a molecular density of  $10^8$  cm<sup>-3</sup>, and an interaction volume of  $5 \times 10^{-6}$  cm<sup>3</sup> the signal on the detector of electrons elastically scattered off an already destroyed molecule is  $S^D \approx 0.5 \cdot S_{\text{elastic}}^D \cdot S_{\text{ionized}}^D = 0.5 \cdot 5 \times 10^{-3} \cdot 5 \times 10^{-4} = 1.25 \times 10^{-6}$  per shot [21]. This corresponds to a fraction of  $P^D = S^D/S_{\text{elastic}}^D = 2.5 \times 10^{-4}$  electrons scattered off damaged molecules per elastically-scattered signal electron. Thus, radiation damage is not relevant in these experiments. Importantly, it is much smaller than in similar x-ray-diffraction experiments, where radiation damage was not necessarily negligible, but could be reduced by increasing the x-ray beam diameter [21].

The current setup could be improved by increasing the acceleration fields: This would simultaneously increase the electron number for the same laser power and lead to a smaller emittance and, thus, an increased coherence length of the electron beam. The time resolution could either be improved through a more compact design and stronger electric fields [33] or by combining the setup with an RF cavity for appropriate phase-space rotation for temporal focusing [30, 31, 50].

In conclusion, a new source for picosecond time-resolved electron diffraction experiments with the need for large numbers of electrons was described. It will allow, for instance, the investigation of dilute samples of controlled gas-phase molecules [12]. Moreover, enabled by its velocity map imaging spectrometer geometry, the setup allowed to characterize the electron beam properties, e. g., the spatial and velocity distributions of the electrons. The focusing and coherence properties of the electron pulses were determined through both, simulations and diffraction experiments of aluminum-foil samples, to be sufficient for the envisioned atomically resolved controlled molecule diffractive imaging.

We thank Sven Lederer, Ingo Hansen, and Hans-Hinrich Sahling for helpful advice regarding the photocathode design and Klaus Floettmann for help with ASTRA simulations. We gratefully acknowledge discussions with Martin Centurion, Jie Yang, Stephan Stern, and Henry N. Chapman on gas-phase aligned-molecule diffraction as well as helpful discussions regarding electron diffraction with Stuart Hayes, German Sciaini, Kostyantyn Pichugin, Julian Hirscht, and Dwayne Miller. We thank Masaki Hada for the preparation of the aluminum sample.

Besides DESY, this work has been supported by the excellence cluster "The Hamburg Center for Ultrafast Imag-

ing – Structure, Dynamics and Control of Matter at the Atomic Scale” of the Deutsche Forschungsgemeinschaft (CUI, DFG-EXC1074) and the European Research Council through the Consolidator Grant 614507-COMOTION. N.L.M.M. gratefully acknowledges a fellowship of the Joachim Herz Stiftung.

\* jochen.kuepper@cfel.de; <https://www.controlled-molecule-imaging.org>

- [1] L. Germer, *Phys. Rev.* **56**, 58 (1939).
- [2] K. Takayanagi, *J. Vac. Sci. Technol. A* **3**, 1502 (1985).
- [3] K. Lonsdale, *Proc. Royal Soc. London A* **123**, 494 (1929).
- [4] A. Yonath, *Annu. Rev. Biophys. Biomol. Struct.* **31**, 257 (2002).
- [5] I. Hargittai and M. Hargittai, *Stereochemical Applications of Gas-Phase Electron Diffraction* (VCH Verlagsgesellschaft, 1988).
- [6] J. C. Williamson, J. M. Cao, H. Ihee, H. Frey, and A. H. Zewail, *Nature* **386**, 159 (1997).
- [7] H. Ihee, V. Lobastov, U. Gomez, B. Goodson, R. Srinivasan, C. Ruan, and A. H. Zewail, *Science* **291**, 458 (2001).
- [8] B. J. Siwick, J. R. Dwyer, R. E. Jordan, and R. J. D. Miller, *Science* **302**, 1382 (2003).
- [9] H. N. Chapman, A. Barty, M. J. Bogan, S. Boutet, S. Frank, S. P. Hau-Riege, S. Marchesini, B. W. Woods, S. Bajt, W. H. Benner, L. W. A., E. Plönjes, M. Kuhlmann, R. Treusch, S. Düsterer, T. Tschentscher, J. R. Schneider, E. Spiller, T. Möller, C. Bostedt, M. Hoener, D. A. Shapiro, K. O. Hodgson, D. van der Spoel, F. Burmeister, M. Bergh, C. Caleman, G. Huldt, M. M. Seibert, F. R. N. C. Maia, R. W. Lee, A. Szöke, N. Timneanu, and J. Hajdu, *Nat. Phys.* **2**, 839 (2006).
- [10] J. C. H. Spence, U. Weierstall, and H. N. Chapman, *Rep. Prog. Phys.* **75**, 102601 (2012).
- [11] A. Barty, J. Küpper, and H. N. Chapman, *Annu. Rev. Phys. Chem.* **64**, 415 (2013).
- [12] Y.-P. Chang, D. Horke, S. Trippel, and J. Küpper, *Int. Rev. Phys. Chem.* (2015), 10.1080/0144235X.2015.1077838, in press, arXiv:1505.05632 [physics].
- [13] F. Filsinger, J. Küpper, G. Meijer, J. L. Hansen, J. Maurer, J. H. Nielsen, L. Holmegaard, and H. Stapelfeldt, *Angew. Chem. Int. Ed.* **48**, 6900 (2009).
- [14] T. Kierspel, D. A. Horke, Y.-P. Chang, and J. Küpper, *Chem. Phys. Lett.* **591**, 130 (2014), arXiv:1312.4417 [physics].
- [15] F. Filsinger, U. Erlekam, G. von Helden, J. Küpper, and G. Meijer, *Phys. Rev. Lett.* **100**, 133003 (2008), arXiv:0802.2795 [physics].
- [16] S. Trippel, Y.-P. Chang, S. Stern, T. Mullins, L. Holmegaard, and J. Küpper, *Phys. Rev. A* **86**, 033202 (2012), arXiv:1208.4935 [physics].
- [17] S. Ryu, R. Stratt, and P. Weber, *J. Phys. Chem. A* **107**, 6622 (2003).
- [18] J. C. H. Spence and R. B. Doak, *Phys. Rev. Lett.* **92**, 198102 (2004).
- [19] S. Pabst, P. J. Ho, and R. Santra, *Phys. Rev. A* **81**, 043425 (2010).
- [20] F. Filsinger, G. Meijer, H. Stapelfeldt, H. Chapman, and J. Küpper, *Phys. Chem. Chem. Phys.* **13**, 2076 (2011).
- [21] J. Küpper, S. Stern, L. Holmegaard, F. Filsinger, A. Rouzee, A. Rudenko, P. Johnsson, A. V. Martin, M. Adolph, A. Aquila, S. Bajt, A. Barty, C. Bostedt, J. Bozek, C. Caleman, R. Coffee, N. Coppola, T. Delmas, S. Epp, B. Erk, L. Foucar, T. Gorkhover, L. Gumprecht, A. Hartmann, R. Hartmann, G. Hauser, P. Holl, A. Hömke, N. Kimmel, F. Krasniqi, K.-U. Kühnel, J. Maurer, M. Messerschmidt, R. Moshhammer, C. Reich, B. Rudek, R. Santra, I. Schlichting, C. Schmidt, S. Schorb, J. Schulz, H. Soltau, J. C. H. Spence, D. Starodub, L. Strüder, J. Thøgersen, M. J. J. Vrakking, G. Weidenspointner, T. A. White, C. Wunderer, G. Meijer, J. Ullrich, H. Stapelfeldt, D. Rolles, and H. N. Chapman, *Phys. Rev. Lett.* **112**, 083002 (2014), arXiv:1307.4577 [physics].
- [22] S. Stern, L. Holmegaard, F. Filsinger, A. Rouzee, A. Rudenko, P. Johnsson, A. V. Martin, A. Barty, C. Bostedt, J. Bozek, R. Coffee, S. Epp, B. Erk, L. Foucar, R. Hartmann, N. Kimmel, K.-U. Kühnel, J. Maurer, M. Messerschmidt, B. Rudek, D. Starodub, J. Thøgersen, G. Weidenspointner, T. A. White, H. Stapelfeldt, D. Rolles, H. N. Chapman, and J. Küpper, *Faraday Disc.* **171**, 393 (2014), arXiv:1403.2553 [physics].
- [23] C. J. Hensley, J. Yang, and M. Centurion, *Phys. Rev. Lett.* **109**, 133202 (2012).
- [24] J. Yang, V. Makhija, V. Kumarappan, and M. Centurion, *Struct. Dyn.* **1**, 044101 (2014).
- [25] H. Stapelfeldt and T. Seideman, *Rev. Mod. Phys.* **75**, 543 (2003).
- [26] L. Holmegaard, J. H. Nielsen, I. Nevo, H. Stapelfeldt, F. Filsinger, J. Küpper, and G. Meijer, *Phys. Rev. Lett.* **102**, 023001 (2009), arXiv:0810.2307 [physics.chem-ph].
- [27] O. Ghafur, A. Rouzee, A. Gijbartsen, W. K. Siu, S. Stolte, and M. J. J. Vrakking, *Nat. Phys.* **5**, 289 (2009).
- [28] P. M. Kraus, D. Baykusheva, and H. J. Wörner, *Phys. Rev. Lett.* **113**, 023001 (2014), arXiv:1311.3923 [physics.chem-ph].
- [29] S. Trippel, T. Mullins, N. L. M. Müller, J. S. Kienitz, R. González-Férez, and J. Küpper, *Phys. Rev. Lett.* **114**, 103003 (2015), arXiv:1409.2836 [quant-ph].
- [30] T. van Oudheusden, P. L. E. M. Pasmans, S. B. van der Geer, M. J. de Loos, M. J. van der Wiel, and O. J. Luiten, *Phys. Rev. Lett.* **105**, 264801 (2010).
- [31] G. Sciaini and R. J. D. Miller, *Rep. Prog. Phys.* **74**, 096101 (2011).
- [32] P. Musumeci, J. T. Moody, C. M. Scoby, M. S. Gutierrez, H. A. Bender, and N. S. Wilcox, *Rev. Sci. Instrum.* **81**, 013306 (2010).
- [33] M. S. Robinson, P. D. Lane, and D. A. Wann, *Rev. Sci. Instrum.* **86**, 013109 (2015).
- [34] C. Gerbig, A. Senftleben, S. Morgenstern, C. Sarpe, and T. Baumert, *New J. Phys.* **17**, 043050 (2015).
- [35] S. Lahme, C. Kealhofer, F. Krausz, and P. Baum, *Struct. Dyn.* **1**, 034303 (2014).
- [36] M. W. van Mourik, W. J. Engelen, E. J. D. Vredenburg, and O. J. Luiten, *Struct. Dyn.* **1**, 034302 (2014).
- [37] A. J. McCulloch, D. V. Sheludko, S. D. Saliba, S. C. Bell, M. Junker, K. A. Nugent, and R. E. Scholten, *Nat. Phys.* **7**, 785 (2011).
- [38] M. Gulde, S. Schweda, G. Storeck, M. Maiti, H. K. Yu, A. M. Wodtke, S. Schäfer, and C. Ropers, *Science* **345**, 200 (2014).
- [39] T. Zuo, A. D. Bandrauk, and P. B. Corkum, *Chem. Phys. Lett.* **259**, 313 (1996).
- [40] C. I. Blaga, J. Xu, A. D. DiChiara, E. Sistrunk, K. Zhang, P. Agostini, T. A. Miller, L. F. DiMauro, and C. D. Lin, *Nature* **483**, 194 (2012).
- [41] Y.-P. Chang, K. Długołęcki, J. Küpper, D. Rösch, D. Wild, and S. Willitsch, *Science* **342**, 98 (2013), arXiv:1308.6538

- [physics].
- [42] S. Trippel, T. Mullins, N. L. M. Müller, J. S. Kienitz, K. Długołęcki, and J. Küpper, *Mol. Phys.* **111**, 1738 (2013), arXiv:1301.1826 [physics.atom-ph].
  - [43] A. T. J. B. Eppink and D. H. Parker, *Rev. Sci. Instrum.* **68**, 3477 (1997).
  - [44] M. Stei, J. von Vangerow, R. Otto, A. H. Kelkar, E. Carras-cosa, T. Best, and R. Wester, *J. Chem. Phys.* **138**, 214201 (2013).
  - [45] A. R. Bainbridge and W. A. Bryan, *New J. Phys.* **16**, 103031 (2014).
  - [46] J. R. Maldonado, P. Pianetta, D. H. Dowell, J. Corbett, S. Park, J. Schmerge, A. Trautwein, and W. Clay, *Astro-phys. Lett. & Comm.* **101**, 231103 (2012).
  - [47] K. Floettmann, "ASTRA, a space charge tracking algorithm," (1997).
  - [48] S. Flügge, *Rechenmethoden der Elektrodynamik*, Aufgaben mit Lösungen (Springer Verlag, 1986).
  - [49] S. Trippel, T. Mullins, N. L. M. Müller, J. S. Kienitz, J. J. Omiste, H. Stapelfeldt, R. González-Férez, and J. Küpper, *Phys. Rev. A* **89**, 051401(R) (2014), arXiv:1401.6897 [quant-ph].
  - [50] F. Fu, S. Liu, P. Zhu, D. Xiang, J. Zhang, and J. Cao, *Rev. Sci. Instrum.* **85**, 083701 (2014).